A high throughput in-situ measurement of heat transfer in successive non-isothermal forming of sheet alloys

Xiaochuan Liu [a], Shaomeng Jin [a], Ming Ming [a], Chuanwei Fan [b], Heli Liu [c,*], Denis J. Politis [d], Mateusz Kopec [e]

[a] *School of Mechanical Engineering, Xi'an Jiaotong University, Xi'an 710049, China*
[b] *State Key Laboratory for Mechanical Behavior of Materials, Xi'an Jiaotong University, Xi'an 710049, China*
[c] *Department of Mechanical Engineering, Imperial College London, London SW7 2AZ, UK*
[d] *Department of Mechanical and Manufacturing Engineering, University of Cyprus, 20537 Nicosia, Cyprus*
[e] *Institute of Fundamental Technological Research, Polish Academy of Sciences, 5b Pawinskiego, 02-106 Warsaw, Poland*

ARTICLE INFO

ABSTRACT

The measurement and control of the heat transfer of sheet alloys in successive non-isothermal forming cycles is crucial to achieve the desired post-form properties and microstructure, which could not as of yet be realized by using traditional test facilities. In the present research, a novel heat transfer measurement facility was designed to generate and subsequently measure the in-situ heat transfer from a sheet alloy to multi-mediums such as forming tools, air, lubricant and coating. More importantly, the facility was able to use a single sheet alloy sample to perform successive non-isothermal forming cycles, and subsequently obtain high throughput experimental results including the temperature evolution, cooling rate, mechanical properties and microstructures of the alloy. The high throughput in-situ heat transfer measurement facility identified that the cooling rate of AA7075 was 152 °C/s and the mechanical strength was over 530 MPa in the 1st forming cycle. However, it decreased to less than the critical value of 100 °C/s in the successive 10th forming cycle, leading to a low mechanical strength of only 487 MPa. The identified variations that occur in the successive non-isothermal forming cycles would improve the consistency and accuracy of part performance in large-scale manufacturing.

1. Introduction

Non-isothermal forming technologies have enabled the manufacture of complex thin-walled components from sheet metals and alloys, which are first heated to elevated temperatures to increase the formability and then transferred to cold forming tools to conduct forming and quenching simultaneously [1–3], as shown in Fig. 1a. Fast light Alloys Stamping Technology (FAST) is such a novel non-isothermal sheet metal forming process, which applies a rapid heating rate to heat an aluminum alloy blank sheet to an elevated temperature that is lower than the solution heat treatment temperature (SHT), followed by forming and quenching [2]. During non-isothermal forming, the microstructure and mechanical properties of the sheet alloys vary significantly due to the plastic deformation and simultaneous rapid quenching by the cold forming tools. For example, the β phase transforms into the α/α'phase and the austenite transforms into martensite in the hot stamping of titanium alloys [4] and high-strength steels [5] respectively, and determines the

mechanical properties of the formed components. Additionally, the precipitation of primary and secondary phases of aluminum alloys depends on the quenching rate, and thus determines whether the mechanical properties could be fully recovered after artificial ageing [6]. It is therefore of great importance to study the heat transfer and temperature fields of the sheet alloys under such non-isothermal forming conditions [7].

The heat transfer between sheet alloys and forming tools has been ideally treated such that the contact surfaces are considered as smooth with a minor thermal resistance. In this case, the heat conduction within the sheet alloys and forming tools calculated by their thermal conductivities dominates the heat transfer path [8]. However, the real contact area is much lower than the apparent contact area due to the roughness of the surface, and it increases with increasing plastic deformation [9,10]. In addition, lubricants and surface coatings are widely used as mediums between the sheet alloys and forming tools in non-isothermal forming [11]. This indicates that the heat actually transfers from the

---

* Corresponding author.
E-mail address: h.liu19@imperial.ac.uk (H. Liu).

(a) Non-isothermal sheet alloy forming

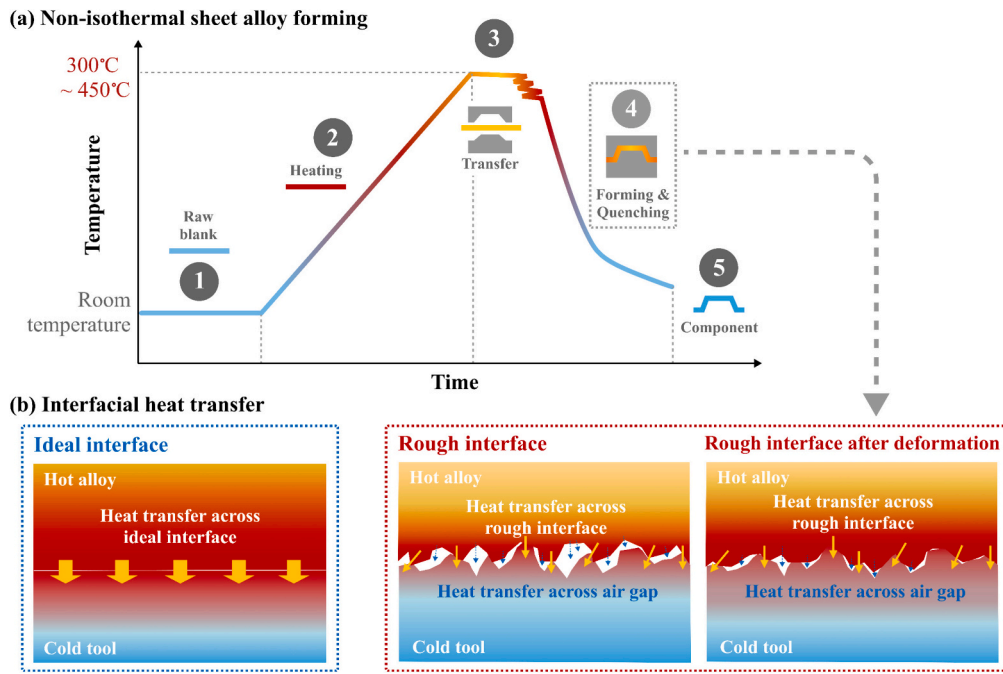**(b) Interfacial heat transfer**

Fig. 1. Schematic diagrams of (a) a non-isothermal sheet alloy forming process; (b) heat transfer from a hot sheet alloy to cold tools across ideal and rough interfaces.
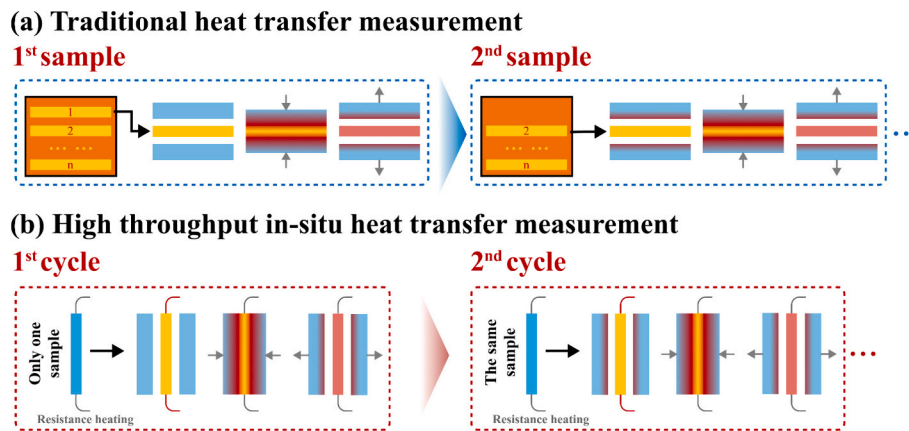
(a) Traditional heat transfer measurement

(b) High throughput in-situ heat transfer measurement

Fig. 2. The design principles of (a) traditional heat transfer measurement and (b) high throughput in-situ heat transfer measurement.

sheet alloys to multi-mediums, i.e. forming tools, air, lubricant and coating, as shown in Fig. 1b. Moreover, considering the scale of industrial mass manufacturing of sheet alloy products, the interfacial conditions such as tool temperature, lubricant film and coating surface would gradually vary in successive forming cycles, consequently affecting the heat transfer of the sheet alloys as well as their plastic deformation, post-form properties and microstructures [12]. Therefore, an in-situ measurement of the heat transfer of sheet alloys in successive non-isothermal forming cycles is critically required to precisely control the temperature fields, post-form properties and material microstructures to improve the consistency and accuracy of part performance in large-scale manufacturing batches [13].

Significant efforts have been made to design test facilities and methods to measure the heat transfer and temperature evolutions of sheet alloys in non-isothermal forming processes. The principle of the measurement is as follows: a sheet alloy sample is first heated in a furnace up to the target temperature, which is monitored by a pair of thermocouples; it is then manually transferred to a position in between an upper and a lower flat tool that are equipped on a hydraulic press machine; the upper tool is activated to move downwards to compress and simultaneously quench the hot sample to room temperature; the temperature evolution of the sheet alloy sample through heating, transfer, loading, quenching until unloading is measured, as shown in Fig. 2a. It is shown that the contact pressure [14], surface roughness [15], tool temperature [16], tool material [17], lubricant [18] and coating [7] are key influential factors in determining the heat transfer and temperature evolutions. Specifically, the quenching rate of the sheet alloys increases with increasing contact pressure but decreases with increasing surface roughness, due to the real contact area between the sheet alloys and forming tool being increased with increasing contact pressure but decreased with increasing surface roughness [10]. The tool temperature increases with increasing forming cycles, thus reducing the quenching rate of the sheet alloys [19]. When a die material, lubricant and coating with a larger thermal diffusivity is applied, the heat transfer of the sheet alloys is enhanced and thus their temperature reduces at a greater rate [20].

However, the previous test facilities are not able to measure the in-situ heat transfer of sheet alloys through heating, transfer, loading, quenching until unloading. Moreover, the measurement of heat transfer terminates after unloading and could not be launched again in a short
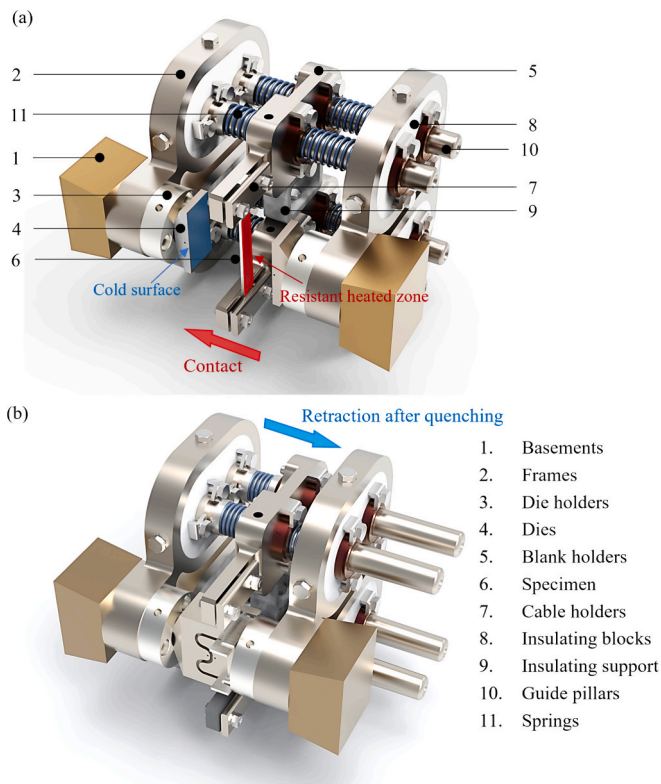
Fig. 3. The high throughput in-situ heat transfer measurement facility for successive non-isothermal forming cycles equipped with (a) flat dies before activation and (b) a pair of M-shaped dies after full compression.

time, thus neglecting the variations in temperature, cooling rate, material properties and microstructures that occur in successive non-isothermal forming cycles. In order to capture those variations, a large number of sheet alloy samples have to be heated in a furnace simultaneously, and a new sample is manually transferred into the position to activate a new cycle after quenching the previous sample. This limitation decreases the control accuracy of the heat transfer and temperature evolutions of the thermal-sensitive materials such as high-strength aluminum alloys [21], dual-phase titanium alloys [22] and magnesium alloys [23], and further degrades the consistency of the material properties and microstructures.

In the present research, a high throughput in-situ heat transfer measurement facility was developed to automatically perform successive non-isothermal forming cycles by using a single alloy blank and then obtain the in-situ temperature evolution of the alloy, the results of which were used to study the cooling rate, post-form mechanical properties and microstructure. Subsequently, successive fast light alloy stamping (FAST) cycles of 7075 aluminum alloy were conducted by using the developed measurement facility, identifying the variations in heat transfer, cooling rate and mechanical strength of the material in different forming cycles. Moreover, the microstructure of AA7075 was observed to investigate the transformation and growth of the precipitates by using transmission electron microscopy (TEM/HRTEM), thus revealing the mechanism of the identified variations during the successive FAST cycles.

2. Design of a high throughput in-situ heat transfer measurement facility

The design of a high throughput in-situ heat transfer measurement facility followed four principles: 1) generation of heat transfer from a sheet alloy to multi-mediums including tools, air, lubricant and coating under different conditions; 2) in-situ measurement of heat transfer of the

sheet alloy during the entire processes; 3) automatic activation of the next cycle immediately once the last cycle terminated to perform successive forming cycles by using a single sheet alloy sample, thus obtaining high throughput experimental results; 4) precise control of processing parameters, such as heating rate, heating temperature, transfer time, contact load/pressure, and quenching time.

The high throughput in-situ heat transfer measurement facility could be assembled with a Gleeble 3800 thermal-mechanical machine, which allowed precise feed-back control of a compression load of up to 20 tons, a heating rate of up to 10,000 °C/s and a forming speed of up to 2000 mm/s. In the heat transfer measurement facility, an alloy specimen was designed to be positioned in between a left and right forming tool and then heated by using electric-resistance heating. The hydraulic system of the Gleeble actuated the forming tools to compress and simultaneously quench the heated specimen. After unloading, the heat transfer measurement facility was able to automatically reset whilst activating the next cycle of heating without changing the alloy specimen, thus obtaining the high throughput results in a single set of testing. Pairs of thermocouples were embedded on the alloy specimen statically to measure the in-situ heat transfer and temperature evolutions during the entire process. The design principles of the high throughput in-situ heat transfer measurement facility are shown in Fig. 2b.

The design rendering of the high throughput in-situ heat transfer measurement facility is shown in Fig. 3. Specifically, Parts 1 were steel basements to connect the facility to the press machine, and their trapezoid geometry was designed to enable seamless assembly with the Gleeble 3800, allowing the hydraulic actuation of the right basement with the left one being static. The geometry of Parts 1 could be adjusted to allow the heat transfer measurement facility to be assembled with other thermal-mechanical machines in addition to Gleeble. Parts 2 were steel frames bolted onto Parts 1 to support the entire sliding system of the measurement facility, and were designed as symmetrical parts to ensure an even distribution of the weight as well as a stable sliding along the horizontal plane. Parts 3 were die holders to connect Parts 4 dies and Parts 2 frames, allowing for easy replacement of the dies, of which the contact surfaces could be either flat with the desired surface roughness, lubricated, or coated to compress the sheet alloys and subsequently study their heat transfer across multi-mediums. Alternatively, the desired shapes of the dies could be manufactured to form the sheet alloys to subsequently study their plastic deformation and post-form properties. For example, a pair of M-shaped dies were designed in the present research and demonstrated in Fig. 2b. In addition, cooling channels could be designed in the die holders.

Parts 5 were symmetrical blank holders that clamped Part 6 an alloy specimen with Parts 7 cable holders to ensure the specimen contacted the center of the dies. The geometry of the specimen that depended highly on the test requirements, could be either a rectangular shape for heat transfer tests only without deformation or a dog-bone shape with notches for complex forming tests to increase stability. Electrical cables were screwed onto the cable holders to enable the resistance heating of the specimen, the center of which the in-situ temperature was measured by pairs of thermocouples at a sampling frequency of 1000 Hz.

Both Parts 8 insulating blocks connecting frames and Part 9 an insulating support were made from an insulating material to prevent a short circuit, connecting the two blank holders through Parts 10 guide pillars. In addition, the insulating support was able to reduce the stress concentration on the four guide pillars, which crossed the blank holders and frames to provide a high stiffness for forming high-strength materials such as titanium alloys and boron steels. Parts 11 were springs mounted on the guide pillars. When compressed by the right frame, the right springs were activated to push the blank holders and specimen towards the die until it was fully closed. Afterwards, the right basement was returned, and the left springs pushed the blank holders and specimen back to their initial positions. Subsequently, the next forming cycle would be activated, thus realizing the multicycle work automatically by using a single specimen. High throughput experimental results,
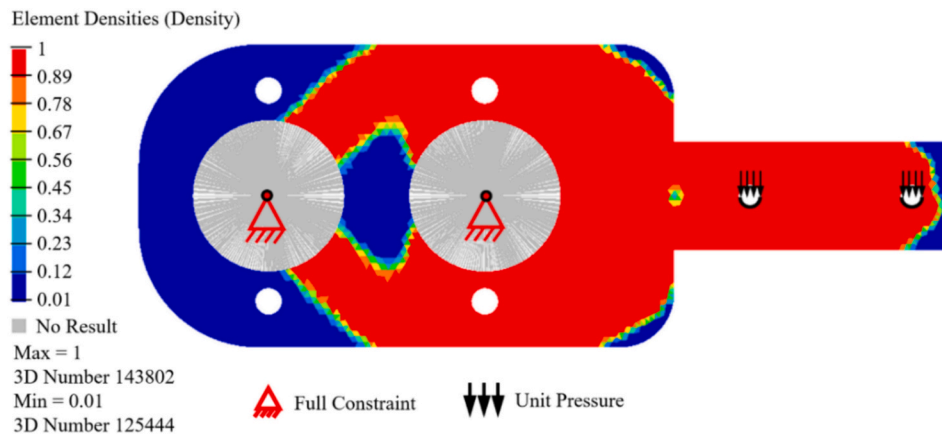
Fig. 4. The boundary condition and relative element density of the blank holders (Part 5).
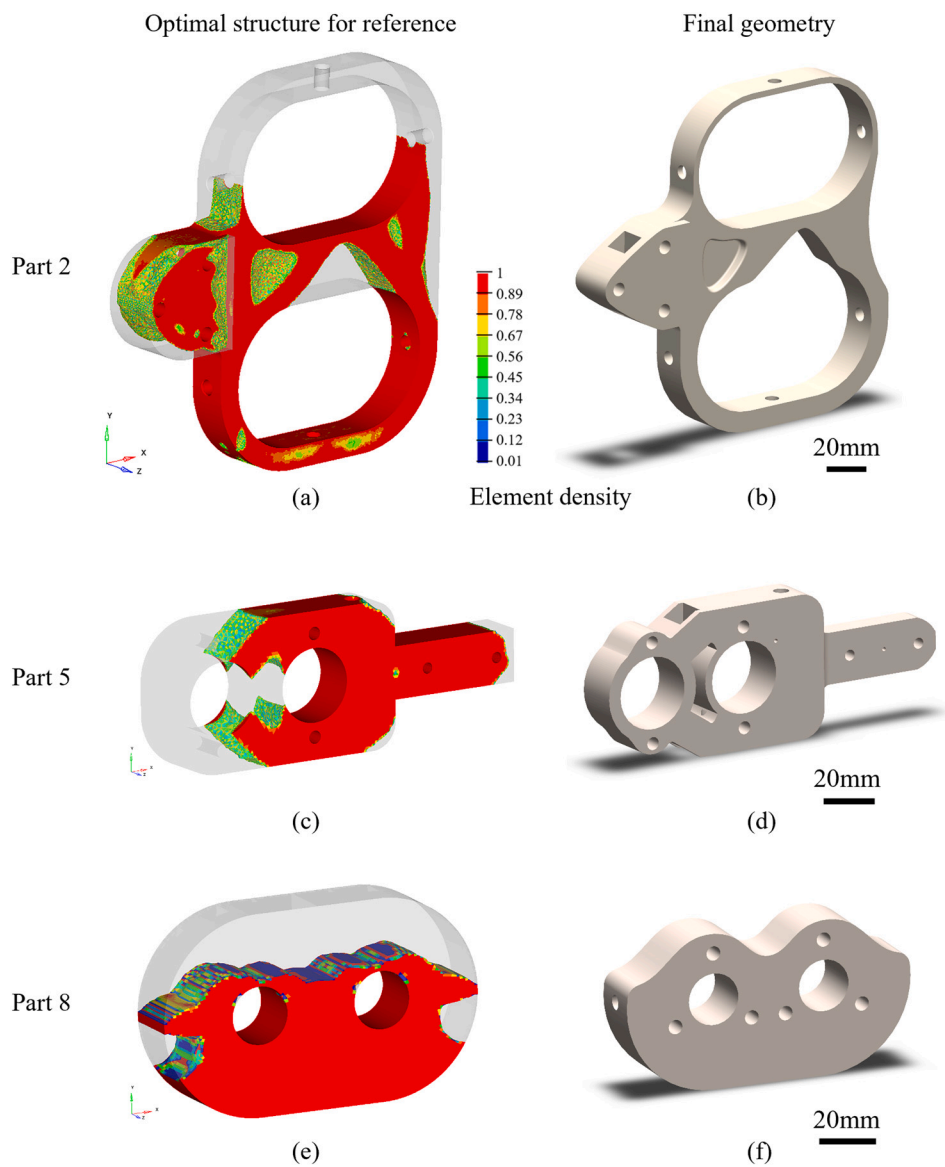

Fig. 5. The optimal structures for reference and final geometries of (a)-(b) the frames (Part 2); (c)-(d) the blank holders (Part 5); (e)-(f) the insulating blocks (Part 8).
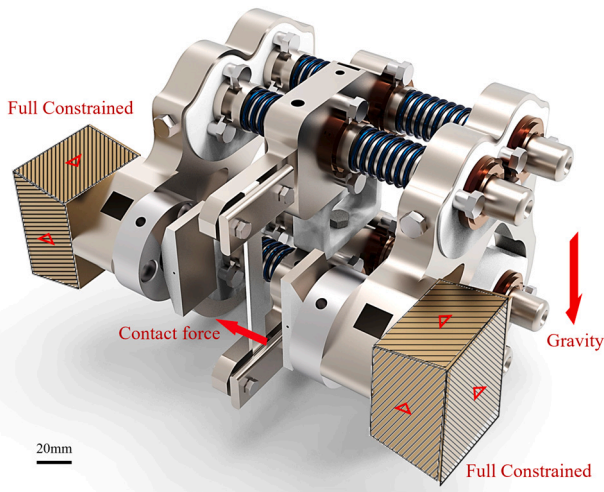
Fig. 6. The topology optimized high throughput in-situ heat transfer measurement facility and its boundary conditions for FEA.

especially the variations in the heat transfer, material properties and microstructures, could therefore be obtained by performing a single set of testing.

After assembly, the work procedure of the developed high throughput in-situ heat transfer measurement facility for successive non-isothermal forming cycles was as follows. A sheet alloy specimen (Part 6) was first clamped between the blank holders (Part 5) and cable holders (Part 7), and then heated up to the target temperature at the desired heating rate. Subsequently, the hydraulic actuation of the Gleeble pushed the right basement (Part 1) joint with the right frame (Part 2), the right insulating blocks (Part 8), the right die holder (Part 3) and the right die (Part 4) along the guide pillars (Part 10) at the defined moving speed. Once compressed between the blank holders and right insulating blocks, the right gas springs (Part 11) pushed the blank holders (Part 5), specimen (Part 6), cable holders (Part 7) and insulating support (Part 9) towards the left die. After the specimen was fully compressed by the dies at the defined closing force and time, the right basement was retracted by the hydraulic actuation and the left gas springs pushed the blank holders back to their initial positions, followed by the activation of a new cycle. Therefore, the developed high throughput in-situ heat transfer measurement facility enabled heating, transfer, loading, quenching and unloading of sheet alloys, and more importantly the automatic activation of the next cycle of heating once unloading finished, thus realizing the successive non-isothermal forming cycles by using a single alloy specimen. The in-situ heat transfer from sheet alloys to multi-mediums including forming tools, air, lubricant and coating could be measured during the entire processes, which could not be performed by using the traditional test facilities.

3. Topology optimization of the high throughput in-situ heat transfer measurement facility

Due to the accommodation limit of the Gleeble chamber, the center of gravity of the high throughput in-situ heat transfer measurement facility was tilted outwards, thus generating a torque. Consequently, a slight deformation of the guide pillars would occur after a period of working, decreasing the testing accuracy and repeatability. Therefore, a topology optimization was applied to reduce the facility weight whilst maintain its stiffness to ensure a long-term service at high working performance.

3.1. Topology optimizing algorithm and scheme

The optimization work was carried out in the *OptiStruct* module of

Altair HyperWorks. Concerning the general optimization constraint, the formulation could be illustrated as Eq. (1):

$$\begin{cases} min f(\mathbf{x}) = (\mathbf{x}_1, \mathbf{x}_2, ..., \mathbf{x}_n) \\ subject \ to : g_j(\mathbf{x}) \leq 0 \ \ j = 1, ..., m \\ x_i^{\min} \leq x_i \leq x_i^{\max} \ \ \ i = 1, ..., n \end{cases} \quad (1)$$

As the designed domain was discretized with a specific number of elements, x_n was defined to represent the objective function as $f(\mathbf{x})$ with the amount of n designed variables. The optimization constraint $g_j(\mathbf{x})$ was considered as satisfied if $g_j(\mathbf{x}) \leq 0$, while it was violated if $g_j(\mathbf{x}) > 0$.

The *OptiStruct* module and solid isotropic material with penalization method (SIMP) were then applied to conduct the topology optimization to reduce the volume and mass of the heat transfer measurement facility without degrading the working performance. According to the SIMP method, each element had a designed variable x_e, which could be described as the 'pseudo (relative) density' from 0 to 1, indicating that the state of the element varied from void to solid. Therefore, the stiffness matrix k_0 was penalized as Eq. (2):

$$k(x_e) = (x_e)^p k_0 \quad (2)$$

Due to a high stiffness of the developed heat transfer measurement facility being necessary to ensure the contact and processing accuracy of the interface under static and loading conditions, the optimization problem had to be constrained to a given volume fraction that was dependent on the ideal weight loss ratio. Therefore, the ordinary problem that maximized the stiffness while minimized the compliance of the developed heat transfer measurement facility, was written as Eq. (3):

$$\begin{cases} \underset{\mathbf{x}}{min} : c(\mathbf{x}) = \mathbf{U}^T \mathbf{K} \mathbf{U} = \sum_{e=1}^{N} (x_e)^P \mathbf{u}_e{}^T \mathbf{k}_0 \mathbf{u}_e \\ subject \ to : \dfrac{v(\mathbf{x})}{v_0} = f \ \ \mathbf{K}\mathbf{U} = \mathbf{F} \ \ 0 < x_{\min} \leq \mathbf{x} \leq 1 \end{cases} \quad (3)$$

where $\mathbf{U}$ and $\mathbf{F}$ were the global displacement and force vectors respectively to calculate the compliance and strain energy of the developed facility, $\mathbf{K}$ was the global stiffness matrix, and $c(\mathbf{x})$ was the compliance of the structure to evaluate the structural stiffness. After the designed domain was discretized, $\mathbf{u}_e$ and $\mathbf{k}_0$ were applied to represent the displacement vector and stiffness matrix of the meshed elements respectively. $\mathbf{x}$ was introduced as the density vector, and thus the density of each element had to be larger than $\mathbf{x}_{\min}$ to avoid the stiffness singularity. In addition, $v(\mathbf{x})$ was the current material volume, v_0 was the volume of the initial designed domain, and f was the prescribed volume fraction.

The designed variables x_e were defined by the properties of the created elements , which were iterated according to the sensitivities of the elements, as shown in Eq. (4). The iterations were automatically performed by the *OptiStruct* module.

$$\frac{\partial c}{\partial x_e} = -p(x_e)^{p-1} \mathbf{u}_e{}^T \mathbf{k}_0 \mathbf{u}_e \quad (4)$$

The stiffness matrix was interpolated with the density of the elements in an exponential form according to the SIMP method, of which the penalization power p strongly affected the discretization of the density. Specifically, a large value of p could reduce the number of intermediate density elements ('grey elements'), resulting in a void-solid ('black and white') material distribution within the solution. However, the stiffness singularity might occur if p was excessive. The function of the parameter 'DISCRETE' in *OptiStruct* was similar to that of the parameter p, which influenced the tendency that converged to a void-solid material distribution structure in each iteration.

To prevent checkerboard patterns of the SIMP method, a filter for the sensitivities was introduced, and thus the element sensitivities were modified in each iteration as Eqs. (5)–(6):
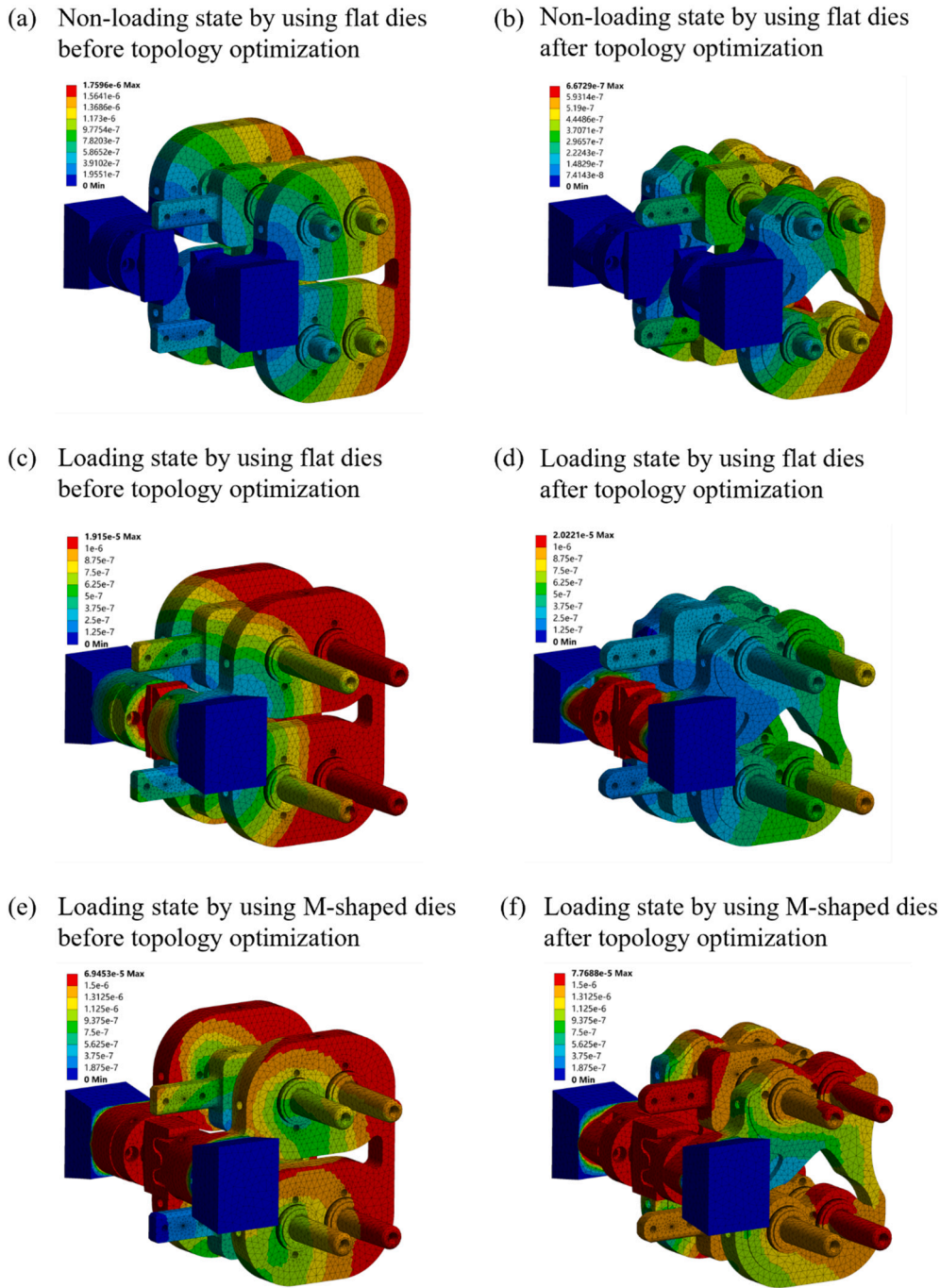
(a) Non-loading state by using flat dies
     before topology optimization

(b) Non-loading state by using flat dies
     after topology optimization

(c) Loading state by using flat dies
     before topology optimization

(d) Loading state by using flat dies
     after topology optimization

(e) Loading state by using M-shaped dies
     before topology optimization

(f) Loading state by using M-shaped dies
     after topology optimization

Fig. 7. The global displacement distributions of the high throughput in-situ heat transfer measurement facility (Unit: m) under different loading conditions.

$$\widehat{\frac{\partial c}{\partial x_e}} = \frac{1}{x_e \sum_{f=1}^{N} \widehat{H}_f} \sum_{f=1}^{N} \widehat{H}_f x_f \frac{\partial c}{\partial x_e} \tag{5}$$

$$\begin{cases} \widehat{H}_f = r_{\min} - dist(e,f) \\ \{f \in N | dist(e,f) \le r_{\min}\}, \mathrm{e} = 1, ..., \mathrm{N} \end{cases} \tag{6}$$

where the weight factor $\widehat{H}_f$ decreased linearly with the variable $dist(e,f)$, which was the distance between the centers of the eth and f^{th} elements. The mechanism of the filter redistributed the sensitivity of each element, avoiding the connection between the rigid nodes. The value of 'CHECKER' (0 or 1) controlled the on-off of the global checkerboard, which would result in a layer of intermediate density elements

remaining at the transition state from solid to void. Therefore, the existence of the checkerboard patterns within the optimized structure determined whether the checkerboard control mechanism was activated or not.

3.2. Topology optimization results and finite element analysis

In order to retain the integrated design, it was necessary to eliminate the dispensable geometrical features, for example a chamfer or fillet, and then rebuild the designed region in *SolidWorks* software. Subsequently, the rebuilt model was imported into *OptiStruct* to discretize the domain and perform the optimization iteration.

The steel frames (Part 2), blank holders (Part 5) and insulating blocks (Part 8) sharing the largest weight (52.2 %) and volume (61.6 %) of the
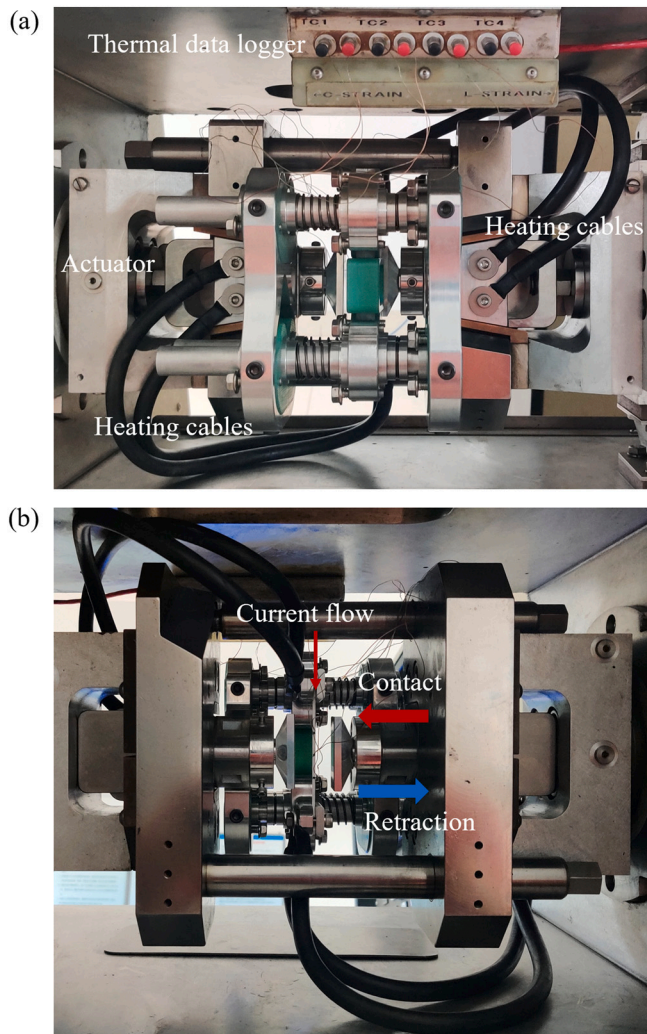
Fig. 8. The assembly of the high throughput in-situ heat transfer measurement facility with a Gleeble 3800 thermal-mechanical machine chamber in (a) front view and (b) back view.

heat transfer measurement facility in total, were the optimization targets of this work. The material property of each part was first defined, i.e. stainless steel for the frame (Part 2) and blank holders (Part 5), and acetal for the insulating blocks (Part 8). The steel frames (Part 2) and blank holders (Part 5) were then meshed with tetrahedral elements to fit the surfaces of curvature, and the insulating blocks (Part 8) were meshed with quadrilateral elements due to the regularity of the designed domain. The mesh size was set as 1 mm to balance the boundary smoothing level and iteration speed. After setting the mesh size and mesh type, each element within the designed domain was assigned with a designed variable (relative density). Therefore, the number of variables would be the same as the number of elements, i.e. Part 2 steel frames: 985985, Part 5 blank holders: 273419, and Part 8 insulating blocks: 110740. The boundary conditions were subsequently defined. For the blank holders (Part 5), the rigid nodes were created and tied with the nodes on the mating surfaces. All the rigid nodes were fully constrained and unit-pressures were applied to each lower half of the two loading holes. For the steel frames (Part 2) and insulating blocks (Part

8), the bottoms of both parts were fully restrained and unit-pressures were applied to the lower half of the mating surfaces inside the part.

Two structural responses were set as the compliance value and volume percentage of the overall structure respectively. According to Eq. 3, the objective function was defined as 'minimal compliance response', and the upper bound of volume fraction response was defined as 0.6, which was conducted as the optimization constraint. To eliminate the 'intermediate density elements' sufficiently, the optimization parameter 'DISCRETE' was set as 3 that was the recommended bound for 3-D solid element, and 'CHECKER' was set as 0 due to no checkerboard pattern being observed. Consequently, the optimal relative element density plot was achieved after iterations (10 steps for Part 2 steel frames, 7 steps for Part 5 blank holders and 8 steps for Part 8 insulating blocks). Taking the blank holders (Part 5) as an example, its boundary condition and optimal relative element density is shown in Fig. 4. Subsequently, the optimal solution was reconstructed in *SolidWorks* software to amend the material removal, ensuring that the functional and process-assembly requirements were met. As a result, the optimal structure references and final geometries of the steel frames (Part 2), blank holders (Part 5) and insulating blocks (Part 8) are shown as Fig. 5, suggesting the weight reduction of 17.7 %, 22.3 % and 22.9 % respectively. Moreover, the weight of the entire heat transfer measurement facility was reduced by 11.8 % from 8.68 to 7.66 kg.

In order to examine the stiffness and working performance after topology optimization, the optimized heat transfer measurement facility assembly was imported into *ANSYS* software to conduct finite element analysis (FEA), the contact regions were automatically detected after import to prevent the parts from penetrating each other. The assembled heat transfer measurement facility was meshed with tetrahedral elements due to their good geometric adaptability. To realize the precise fitting of the elements to the geometry whilst enhancing the computational speed, the size function was defined as 'adaptive', the transition speed was defined as 'slow', and the quality of smoothing was defined as 'medium', resulting in more than 1.2 million elements within the overall structure. Two loading states were subsequently FE analyzed. Specifically, for the non-loading state, the steel basements (Part 1) were constrained, and only the gravity of the measurement facility was considered, as shown in Fig. 6. For the loading state, a pair of die (Part 4) were closed and compressed the alloy specimen (Part 6) at a defined load of 5 MPa, and a pressure was then applied on the contacting surfaces of the dies.

The global displacement distributions of the high throughput in-situ heat transfer measurement facility were simulated to evaluate the stiffness under both the non-loading and loading states. It was shown that the maximum displacement was significantly reduced by 62 % from 1.76 to 0.67 µm under the non-loading state after topology optimization due to the evident weight loss, as shown in Fig. 7 (a and b). In contrast, the displacement slightly increased by 6 % from 19.1 to 20.2 µm under the loading state when using the dies with flat surfaces after topology optimization, as shown in Fig. 7 (c and d). The displacement increased by 12 % from 69.5 to 77.7 µm when using the M-shaped dies, as shown

Table 2
The processing parameters of a FAST cycle.

Parameter	Forming temp.	Heating rate	Contact pressure	Quenching period	Cycle time	No. of cycle
Value	450 °C	50 °C/s	5 MPa	5 s	15 s	12

Table 1
The chemical compositions of the supplied AA7075 in weight proportion (wt%).

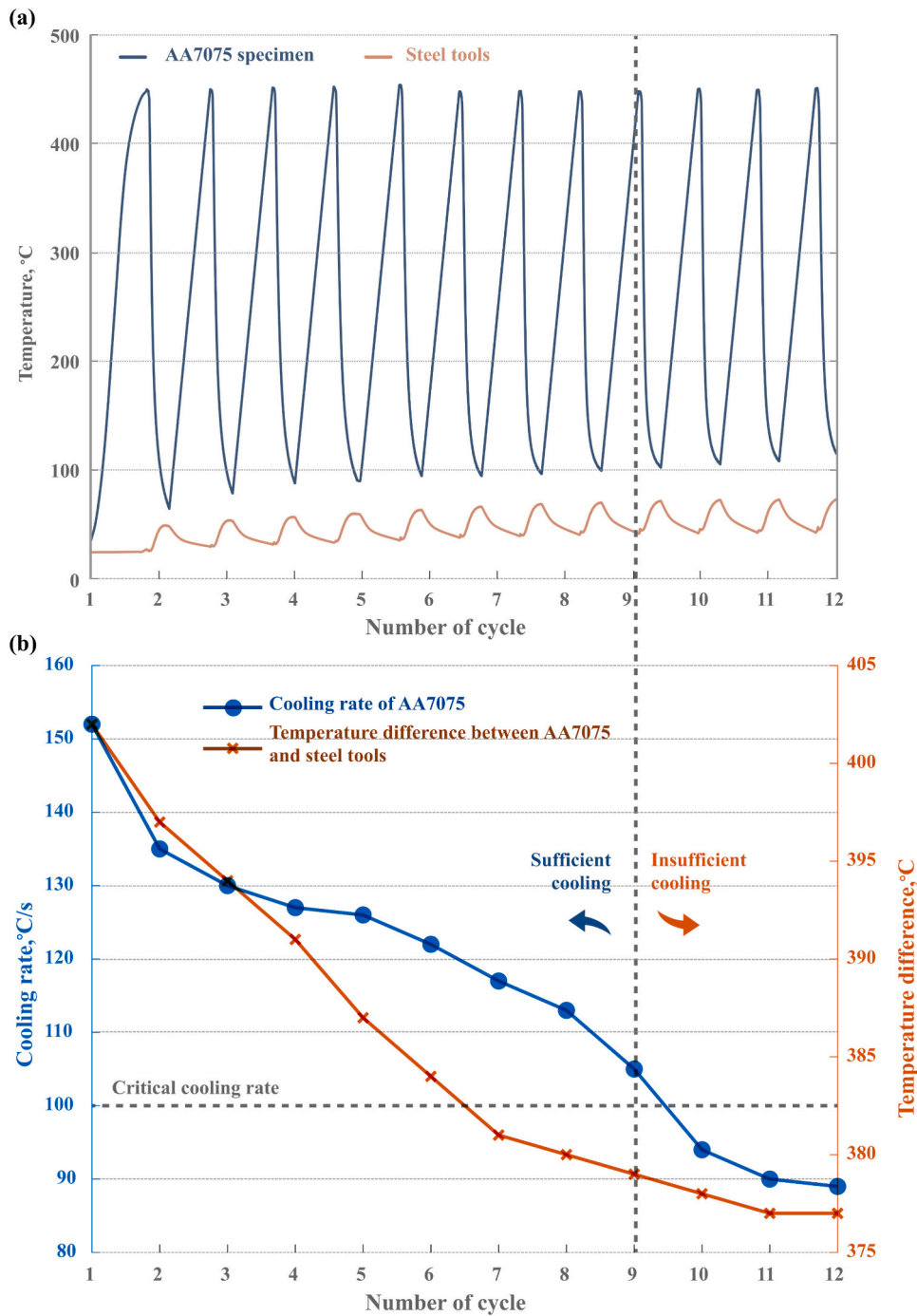| Composition	Si	Fe	Cu	Mn	Mg	Cr	Zn	Ti	Al
Weight %	0.4	0.5	1.5	0.3	2.5	0.22	5.6	0.2	88.78

(a)

(b)

Fig. 9. (a) Temperature evolution and (b) cooling rate of AA7075 in the 12 successive FAST cycles.

in Fig. 7 (e and f). This indicated that the 11.8 % reduction of the weight had a negligible effect on the stiffness and working performance. Moreover, the displacement (shown in red) at the clamped end was significantly reduced under the loading state after topology optimization, proving that the stability of the positioning was greatly improved, as shown in Fig. 7 (c and d). A similar trend was also observed when the M-shaped dies were used, as shown in Fig. 7 (e and f). The topology optimization was applied to reduce the weight of the heat transfer measurement facility as much as possible while maintaining its performance. Therefore, an 11 % weight reduction was significant that ensured a high working performance at a long-term service life. Therefore, the applied topology optimization method and results were reliable to the developed high throughput in-situ heat transfer measurement

facility for the successive non-isothermal forming processes.

4. Experimental procedures of the high throughput in-situ measurement of heat transfer in successive non-isothermal forming cycles

The developed high throughput in-situ heat transfer measurement facility was manufactured and assembled with a Gleeble 3800 thermal-mechanical machine shown in Fig. 8 to conduct 12 successive FAST cycles of 2 mm thick pre-tempered AA7075, of which the chemical compositions provided by Novelis Ltd. are shown in Table 1. Specifically, an AA7075 specimen was first heated to 450 °C at a heating rate of 50 °C/s and then flat steel tools at room temperature moved towards
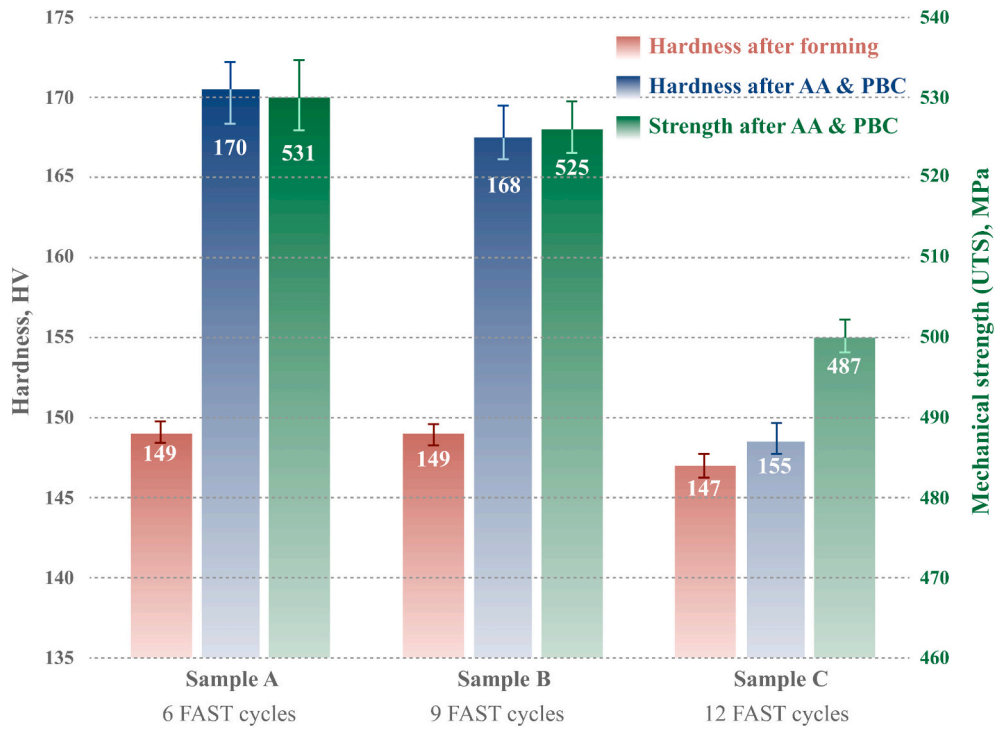
Fig. 10. Hardness and mechanical strength (UTS) of specimen A (6 FAST cycles), B (9 FAST cycles), and C (12 FAST cycles) after forming and artificial ageing+PBCs (AA & PBC).
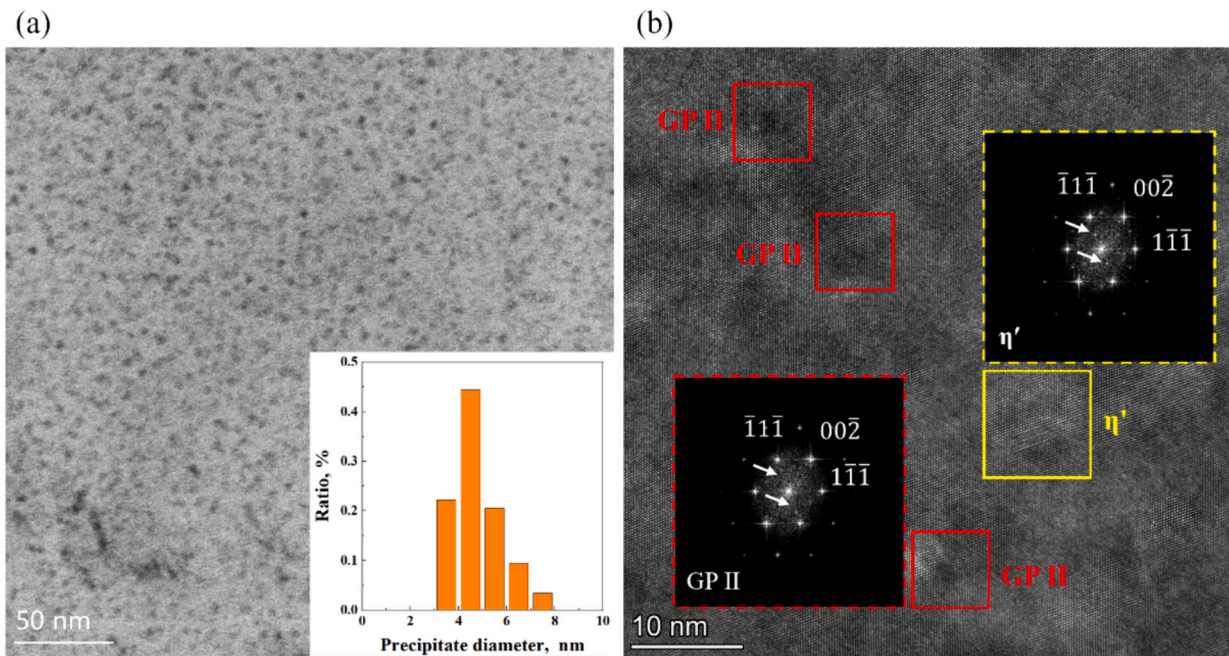

Fig. 11. (a) TEM micrograph and size distribution of the as-received AA7075; (b) HRTEM micrographs and FFT patterns of GPII zone and η' phase.

the hot specimen at a speed of 100 mm/s, followed by the compression at a pressure of 5 MPa for 5 s. Once the flat tools were retracted, a new cycle was activated immediately without changing the specimen, resulting in a cycle time of approximately 15 s. The processing parameters are shown in Table 2. In addition to 12 successive FAST cycles, 6 and 9 successive cycles were also conducted by using different AA7075 samples to study the variations in heat transfer, cooling rate, mechanical strength and microstructure during different forming cycles.

The in-situ heat transfer and temperature evolution of AA7075 was

measured by pairs of thermocouples statically during the successive FAST cycles, the results of which could be used to study the quenching behavior and cooling rate of the material. Subsequently, uniaxial tensile tests were conducted to measure the mechanical strength (ultimate tensile strength UTS) of AA7075 at room temperature and a strain rate of 0.001 s^{-1} (equivalent to 3.6 mm/min) by using a universal testing machine. In addition, the hardness of AA7075 was measured at a load of 9.8 N (equivalent to HV1) by using a digital micro Vickers hardness tester. The microstructure of the material was observed by using a Talos
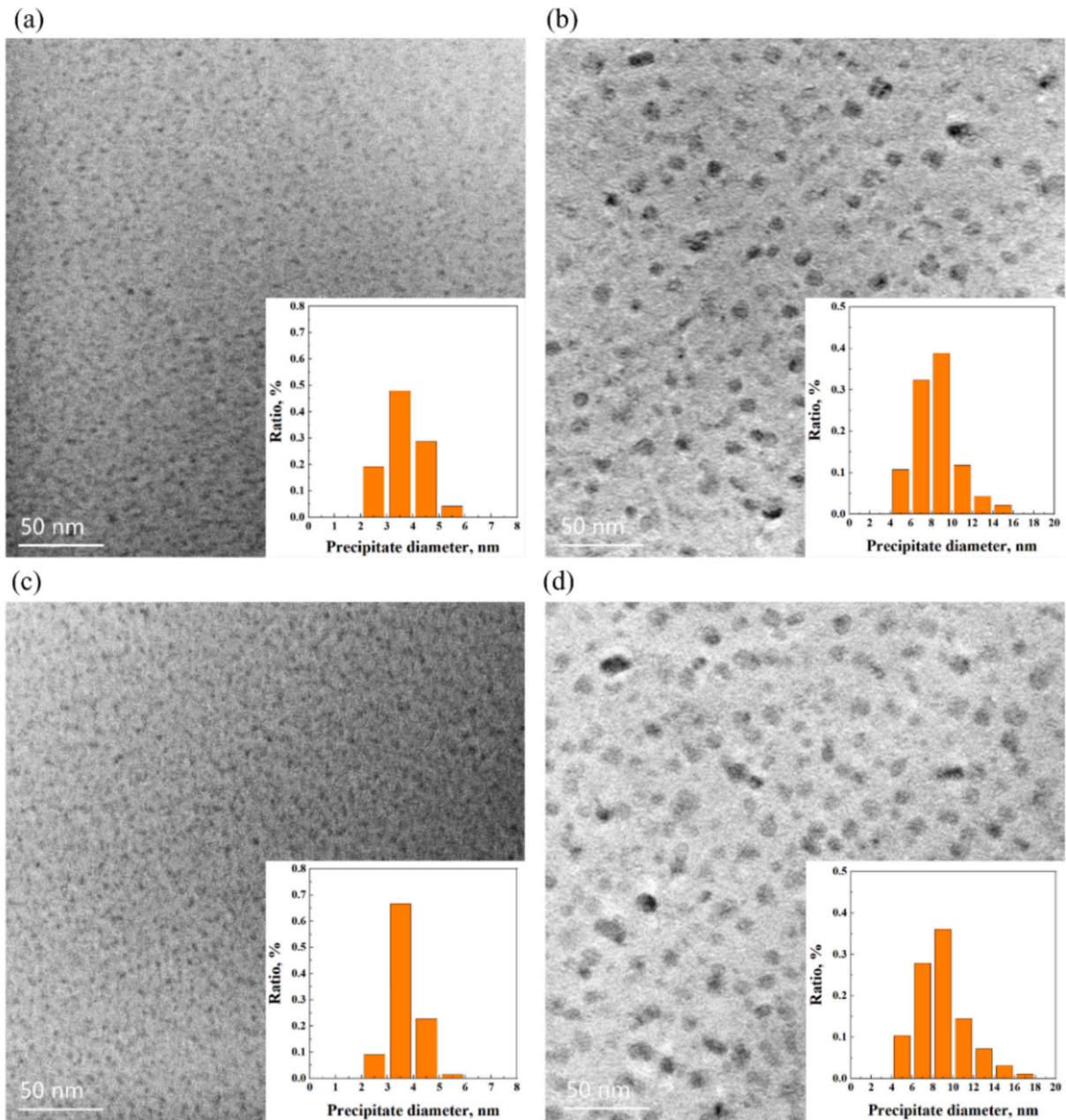
Fig. 12. TEM micrographs with the size distributions of the precipitates of specimen A (a) after 6 FAST cycles, and (b) after artificial ageing+PBCs; specimen B (c) after 9 FAST cycles, and (d) after artificial ageing+PBCs.

F200i transmission electron microscopy (TEM) and a Jeol JSM-F200 high resolution transmission electron microscopy (HRTEM), of which the sample was first electropolished at a temperature of 273 K and a working voltage of 30 V was applied in an electrolyte mixture of 10 % perchloric acid and 90 % ethanol. A Gatan 691 Precision Ion Polishing system was then used to thin the sample to 30 μm at an accelerating voltage between 1.5 and 4 keV, and a sputtering angle between 5° and 10°.

5. Results and discussion

5.1. Heat transfer and quenching behavior of AA7075 in the successive FAST cycles

The heat transfer and temperature evolutions of the central AA7075 specimen and steel tools during the 12 successive forming cycles were obtained, as shown in Fig. 9. In addition to those in the first cycle where the heating rate was reduced to 10 °C/s after 420 °C to avoid over-shooting, the forming temperature was precisely controlled at 450 °C ± 5 °C and the heating rate was 50 °C/s ± 2 °C/s in the other 11 cycles, proving a good repeatability and stability of the high throughput in-situ heat transfer measurement facility. However, the temperature evolution of the tools and cooling rate of AA7075 varied in different cycles. Specifically, the peak temperature of the tools increased from 49 °C in the 1st cycle to 72 °C in the 10th cycle and was maintained in the last two cycles. In order to study the effect of tool temperature on the quenching behavior of AA7075, the average cooling rates in the 12 successive FAST cycles were calculated at the range between 450 °C and 120 °C, of which the lower temperature had negligible influence on the precipitation [24].

The cooling rate of AA7075 decreased from 152 °C/s in the first cycle to 107 °C/s in the 9th cycle and became less than the critical value of
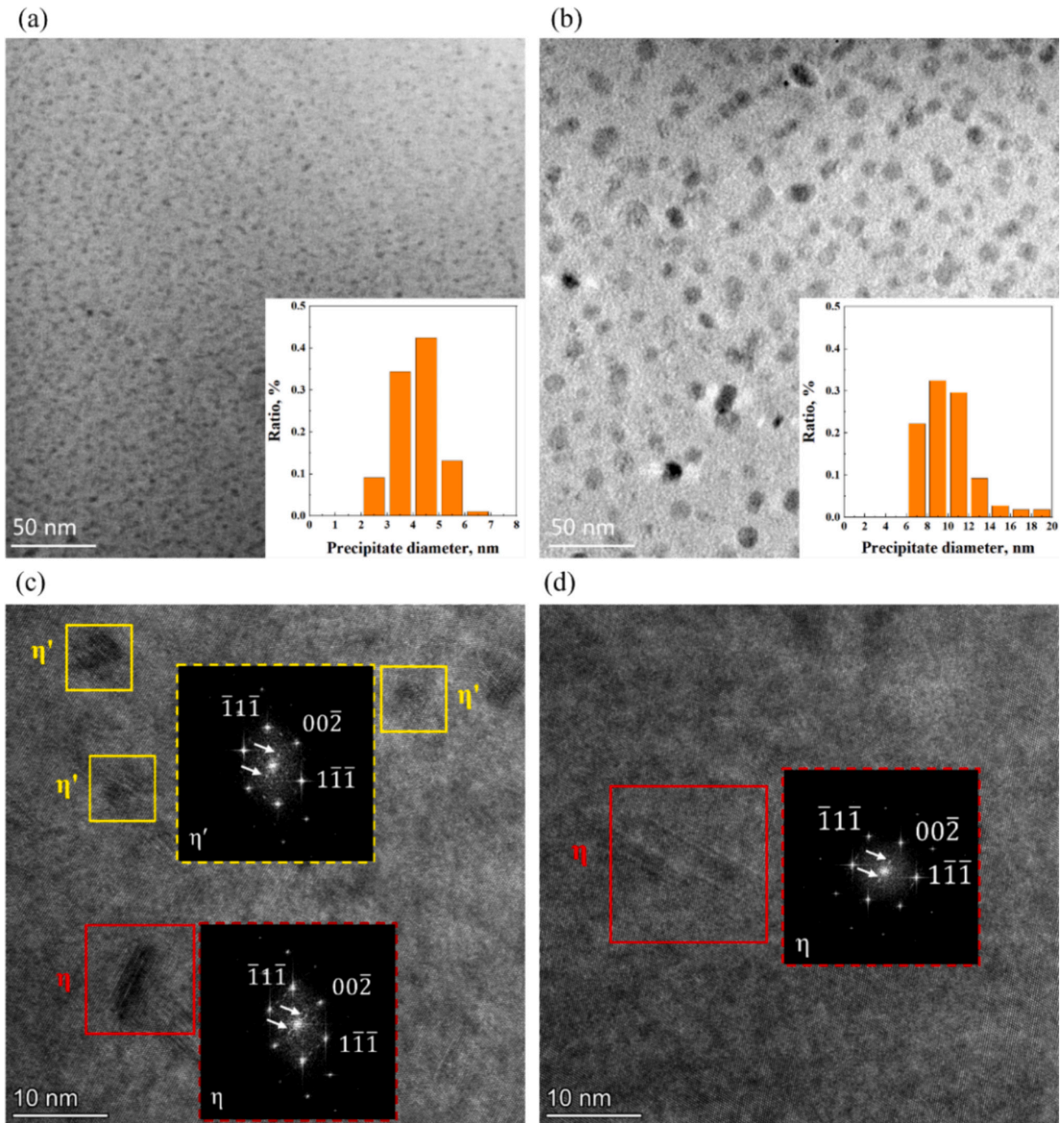
Fig. 13. TEM micrographs with the size distributions of the precipitates of specimen C (a) after 12 FAST cycles and (b) after artificial ageing+PBCs; HRTEM micrograph and FFT pattern of (c) η' and (d) η phases of specimen C after artificial ageing+PBCs.

100 °C/s since the 10th cycle, indicating that coarse particles precipitated in the aluminum grains and primary precipitates would not be distributed homogenously, thus reducing the mechanical strength [25,26]. Therefore, the increasing tool temperature decreased the thermal gradient and thus the cooling rate of AA7075, resulting in a reduction on the post-form properties. Consequently, coolants/lubricants had to be replenished to enhance the heat transfer between AA7075 and steel tools after 9 forming cycles [27].

5.2. Mechanical strength and microstructure of AA7075 in the successive FAST cycles

In addition to the AA7075 specimen (specimen C) that experienced the 12 successive FAST cycles, another two specimens (namely specimen A and B) were used to conduct 6 and 9 successive FAST cycles respectively, followed by the measurement of the hardness. An artificial ageing (90 mins at 120 °C) and two paint bake cycles (20 mins at 180 °C) required by an auto manufacturer were subsequently applied to those three specimens, of which the hardness and mechanical strength (UTS) were measured again. Two-step artificial ageing of AA7075 can significantly reduce the ageing period [28]. The first step of artificial ageing
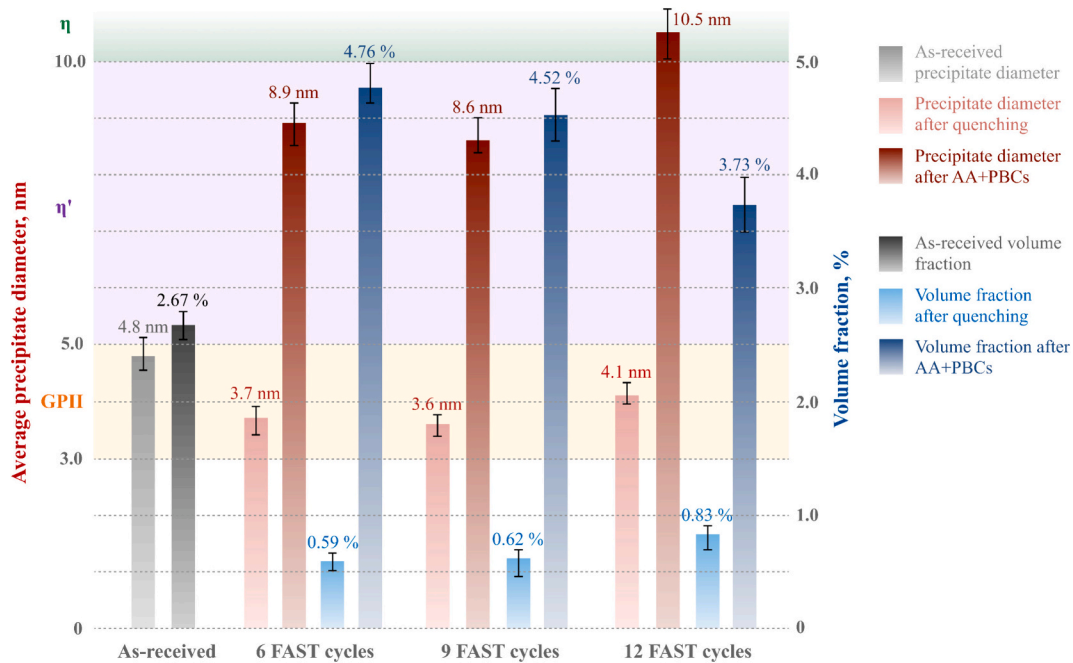
Fig. 14. The average size in diameter and volume fraction of the precipitates of AA7075 after different successive FAST forming cycles.

was conducted at 120 °C for 90 min, which generated numerous GPII zones and a few η' phases. This allowed formed AA7075 to be stored under natural conditions, minimizing the effect of natural ageing. Subsequently, two PBCs equivalent to the second step of artificial ageing, transformed all GPII zones into dispersed η' phases, thereby restoring the mechanical strength of AA7075. For some auto manufacturers, components can be assembled after the first step of artificial ageing with the mechanical strength of vehicle bodies being fully recovered after two PBCs, thus saving the second step of artificial ageing.

As shown in Fig. 10, the hardness values of specimens A, B and C after the successive FAST cycles were similar, reaching approximately 148 HV. After artificial ageing (AA) and paint bake cycles (PBC), the hardness of specimens A and B increased to 170 and 168 HV respectively, and their mechanical strengths were 531 and 525 MPa, which were no less than 90 % of that of AA7075 at the T6 temper (180 HV in hardness and 580 MPa in mechanical strength UTS). However, the hardness and mechanical strength of specimen C was 155 HV and 487 MPa respectively after artificial ageing and PBCs, which were much lower than those of specimens A and B. This indicated that the hardness/ mechanical strength of AA7075 could not be highly recovered if the critical cooling rate of 100 °C/s was not reached during quenching. It should be noted that a mechanical strength exceeding 90 % of that of AA7075 at T6 temper could be achieved by using an artificial ageing for a duration longer than 90 mins, when the critical cooling rate was met.

The as-received AA7075 material was obtained from the supersaturated solid solution (SSSS) after conducting a pre-ageing process at a temperature of 120 °C, and its microstructure was first observed by using TEM, as shown in Fig. 11a. The precipitates were dispersedly distributed with a volume fraction of 2.67 %, and their sizes followed Gaussian distribution with an average value of 4.8 nm in diameter, which was close to that of a GPII zone (3 to 5 nm) and smaller than that of an η' phase (5 to 10 nm) [29,30]. Therefore, it was suggested that the microstructure of the as-received AA7075 was a mixture of numerous GPII zones and a few η' phases. Subsequently, HRTEM with fast Fourier transform (FFT) pattern was used to characterize the structures of the precipitates, as shown in Fig. 11b. The platelet precipitates showed by the sharp streaking along the {111} direction were identified as the GPII zone [31,32], and that showed the weak diffraction spots at 1/3 and 2/3 positions along the {111} direction which was identified as the η' phase

[33,34].

The microstructures of specimens A and B after performing the successive FAST cycles were subsequently observed, as shown in Fig. 12 (a and c). It was found that the volume fraction of the precipitates of the two specimens was significantly decreased to 0.59 % and 0.62 % respectively, indicating that the majority of the GPII zones and η' phases were dissolved at a forming temperature of 450 °C and at a cooling rate of over 100 °C/s. In the subsequent artificial ageing and PBCs, a large amount of GPII zones precipitated and then transformed into η' phases, dominating the microstructure of AA7075. Fig. 12 (b and d) showed the volume fraction of the precipitates of specimens A and B increased to 4.76 % and 4.52 % respectively after artificial ageing and PBCs, and the average diameter of the precipitates increased to 8.9 and 8.6 nm respectively, which was within the range of the size of η'. This indicated the dominant metastable strengthening η' phases. It should be noted that the forming temperature of 450 °C was applied to increase the formability of AA7075 to form complex-shaped components, thus requiring an artificial ageing process of 90 mins at 120 °C to be applied. When an optimal forming temperature range between 300 °C and 350 °C was used, the mechanical strength of AA7075 could be fully recovered after conducting PBCs without any artificial ageing [35].

The TEM micrograph of specimen C after 12 successive FAST cycles demonstrated the volume fraction of the precipitates of 1.38 % and the size distribution of the precipitates with the average value of 4.1 nm in diameter, as shown in Fig. 13a. Although the majority of the precipitates dissolved, some coarse η' phases remained and over-aged η phases precipitated that were stronger than GPII zones, when the cooling rate was less than 100 °C/s. This was the reason that the hardness of specimen C was slightly lower than those of specimens A and B after forming. As shown by the HRTEM and FFT pattern in Fig. 13 (c and d), the coarse particle incoherent with the aluminum matrix with the diffraction spot at 1/2 of the {111} positions was characterized as the η phase [36,37]. Consequently, the transformation from GPII zones to η' phases as well as from the pre-existing η' phases to η phases, and the growth of the preexisting η' and η phases were simultaneously occurred in the following artificial ageing and PBCs. As a result, the strengthening phases of AA7075 contained coarse η' phases and over-aged η phases, of which the size varied significantly from 6 to 20 nm in diameter shown in Fig. 13b, excessively occupying the aluminum matrix. This was the
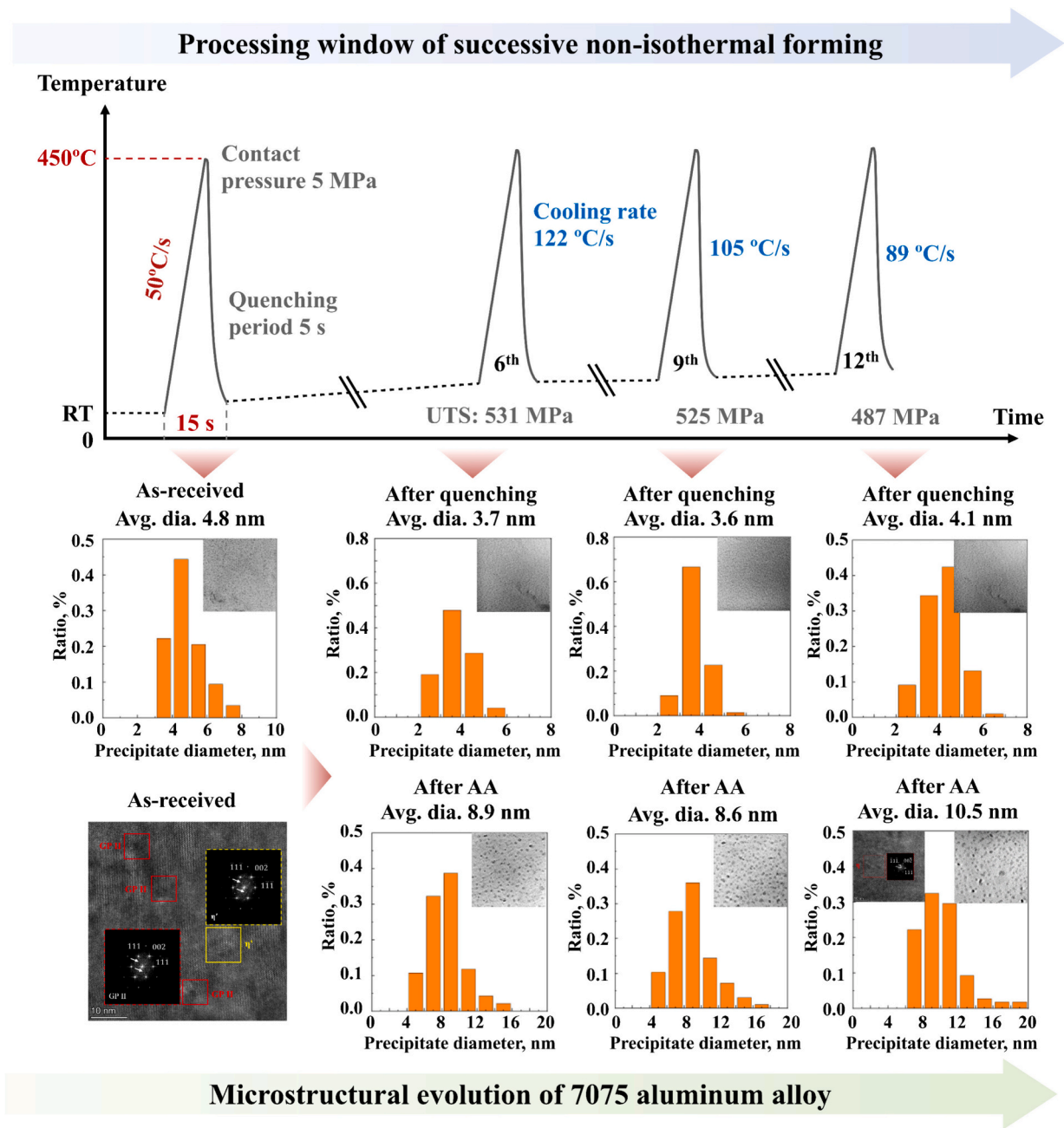
Fig. 15. Schematic diagram of the processing window and microstructural evolution of the AA7075 during the successive FAST cycles (TEM micrographs derived from Figs. 11–13).

reason that the mechanical hardness of specimen C was much lower than those of specimens A and B after artificial ageing and PBCs.

The average size in diameter and volume fraction of the precipitates of AA7075 under different conditions are summarized in Fig. 14. The average size of the precipitates decreased from 4.8 nm to approximately 3.8 nm after the successive 6 and 9 FAST cycles, remaining in the range of the size of GPII zones. Meanwhile, the precipitate volume fraction decreased from 2.67 % to approximately 0.6 %, indicating the great dissolution of the pre-existing precipitates. After artificial ageing and PBCs, the average size of the precipitates significantly increased to approximately 8.8 nm, reaching the range of the size of η' phases. The volume fraction of the precipitates increased to approximately 4.6 %, approaching the value under the T6 temper of AA7075. Although the precipitate size of 4.1 nm was within the range of the size of GPII zones, a few coarse η' phases and over-aged η phases precipitated after the

successive 12 FAST cycles. The average size of the precipitates increased to 10.5 nm after artificial ageing and PBCs, exceeding the range of the size of η' phases. In addition, the volume fraction of 3.73 % was much lower than the value under the T6 temper of AA7075, proving that the coarse precipitates excessively occupied the aluminum matrix and thus reduced the mechanical strength of the material. Therefore, the microstructure results verified that the dispersed distribution of the metastable η' phases and thus the peak mechanical strength/hardness of AA7075 could be achieved only when the critical cooling rate of 100 °C/s was satisfied after no more than 9 successive FAST cycles. In addition, the deterioration of the mechanical strength/hardness of AA7075 would be more severe with additional forming cycles being applied.

The present study validated that the developed facility was capable of automatically activating the next cycle of heating after unloading without changing the specimen and thus measuring the in-situ heat

transfer and temperature evolutions of sheet aluminum alloys during the successive non-isothermal forming cycles at a good accuracy and repeatability. The experimental results revealed the mechanism of the variations in heat transfer, cooling rate, post-form properties and material microstructure as well as provided a guidance on the precise control and improvement of part performance for large scale multi-cycle manufacturing. Specifically, the microstructure of AA7075 was maintained as a mixture of numerous GPII zones and a few η' phases when quenched at a cooling rate greater than 100 °C/s before 9 successive FAST cycles, resulting in the dispersed distribution of η' phases and the mechanical strength of no less than 90 % of that of AA7075 at the T6 temper (580 MPa) after artificial ageing/PBCs. However, the cooling rate decreased with increasing forming cycle and the critical value of 100 °C/s could not be satisfied since the 10th cycle, leading to the precipitation of a few coarse η' phases and over-aged η phases after quenching. Consequently, the mechanical strength of AA7075 could not be recovered after artificial ageing/PBCs. A schematic diagram of the revealed mechanism during the successive FAST cycles is shown in Fig. 15.

6. Conclusions

A high throughput in-situ heat transfer measurement facility was developed in the present research to automatically perform the successive non-isothermal forming cycles by using a single alloy blank and then measuring the in-situ heat transfer from the sheet alloy to multi-mediums during the entire forming process. The variations in temperature evolution, mechanical strength and microstructure of the sheet alloy during successive forming cycles were therefore identified. The findings are summarized as follows:

(1) 12 successive fast light alloy stamping (FAST) cycles were conducted to measure the in-situ temperature evolutions of AA7075, of which the forming temperature of 450 °C, heating rate of 50 °C/s and cycle time of 15 s were precisely controlled, validating the reliable repeatability and stability of the developed facility.

(2) The cooling rate of AA7075 decreased with increasing forming cycles and was less than the critical value of 100 °C/s after the 10th cycle, resulting in the mechanical strength of 487 MPa that was much lower than the peak value (580 MPa) after artificial ageing and PBCs.

(3) The majority of the precipitates of AA7075 dissolved after quenching at a rate greater than 100 °C/s. Subsequently, the η' phases were dispersedly distributed with an average diameter of 8.9 nm and a volume fraction of 4.6 % after artificial ageing and PBCs.

(4) A few η' and η phases existed when quenched at a rate slower than 100 °C/s. After the subsequent artificial ageing and PBCs, the η' phases and over-aged η phases with various sizes occupied the aluminum matrix, thus leading to a low mechanical strength.

CRediT authorship contribution statement

Xiaochuan Liu: Writing – review & editing, Writing – original draft, Resources, Funding acquisition, Formal analysis, Conceptualization. **Shaomeng Jin:** Software, Methodology, Investigation. **Ming Ming:** Methodology, Investigation. **Chuanwei Fan:** Validation. **Heli Liu:** Writing – review & editing, Visualization, Supervision, Project administration, Data curation. **Denis J. Politis:** Writing – review & editing, Formal analysis. **Mateusz Kopec:** Writing – review & editing, Formal analysis.

Declaration of competing interest

The authors declare that they have no known competing financial interests or personal relationships that could have appeared to influence the work reported in this paper.

References

[1] Lin J, Dean TA, Garrett RP, Foster AD. Process for forming metal alloy sheet components. 2008.

[2] Wang L, El Fakir O, Sun Y, Ji K, Luan X, Cai Z, et al. A method of forming parts from sheet metal. WO 2019/03556 A1. 2019.

[3] Atxaga G, Arroyo A, Canflanca B. Hot stamping of aerospace aluminium alloys: automotive technologies for the aeronautics industry. J Manuf Process 2022;81: 817–27. https://doi.org/10.1016/j.jmapro.2022.07.032.

[4] Mu Y, Yang X, Wang B, Qu H, Chen F. A novel triple-layer hot stamping process of titanium alloy TC4 sheet for enhancing formability and its application in a plug socket part. Int J Light Mater Manuf 2023;6:189–97. https://doi.org/10.1016/j.ijlmm.2022.10.003.

[5] Chen W, Zhao W, Gao P, Li F, Kuang S, Zou Y, et al. Interaction between dislocations, precipitates and hydrogen atoms in a 2000 MPa grade hot-stamped steel. J Mater Res Technol 2022;18:4353–66. https://doi.org/10.1016/j.jmrt.2022.04.094.

[6] Lin X, Cao L, Wu X, Tang S, Zou Y. Precipitation behavior of spray-formed aluminum alloy 7055 during high temperature aging. Mater Charact 2022;194: 112347. https://doi.org/10.1016/j.matchar.2022.112347.

[7] Wen S, Chen Z, Qu S, Tang JJ, Han X. Investigations on the interfacial heat transfer coefficient during hot stamping of ultra-high strength steel with Al-Si coating. Int J Heat Mass Transf 2022;189:122739. https://doi.org/10.1016/j.ijheatmasstransfer.2022.122739.

[8] Vogel J. A simple inverse heat conduction optimization. Int J Heat Mass Transf 1993;36:4215–20.

[9] Liu X, Ji K, El Fakir O, Fang H, Gharbi MM, Wang L. Determination of interfacial heat transfer coefficient for a hot aluminium stamping process. J Mater Process Technol 2017;247:158–70. https://doi.org/10.1016/j.jmatprotec.2017.04.005.

[10] Buchner B, Buchner M, Buchmayr B. Determination of the real contact area for numerical simulation. Tribol Int 2009;42:897–901. https://doi.org/10.1016/j.triboint.2008.12.009.

[11] Yang X, Liu H, Dhawan S, Politis DJ, Zhang J, Dini D, et al. Digitally-enhanced lubricant evaluation scheme for hot stamping applications. Nat Commun 2022;13: 1–9. https://doi.org/10.1038/s41467-022-33532-1.

[12] Schell L, Sellner E, Heller B, Wenzel T, Groche P. Reliable determination of interfacial heat transfer coefficients for hot sheet metal forming. CIRP Ann 2024; 00:5–8. https://doi.org/10.1016/j.cirp.2024.03.007.

[13] Li J, Tong C, Zhang R, Shi Z, Lin J. A data-informed review of scientific and technological developments and future trends in hot stamping. Int J Light Mater Manuf 2024;7:327–43. https://doi.org/10.1016/j.ijlmm.2023.11.003.

[14] Fan Y, Yang Z, Liu Y, Zhang H, Li Y. Testing and identification method for the interfacial heat transfer coefficient between CFRTP and tools under fast hot-stamping conditions. Int J Heat Mass Transf 2024;226:125494. https://doi.org/10.1016/j.ijheatmasstransfer.2024.125494.

[15] Su X, Song Z, Zhang Z. Interfacial heat transfer coefficient of aluminum alloy in contact solid solution treatment process. Trans Nonferrous Met Soc China 2024;34: 453–64. https://doi.org/10.1016/S1003-6326(23)66410-6. English Ed.

[16] Singh AR, Bhattacharya AS, Butcher C, Daun KJ. Experimental artefacts affecting characterization of the evolving interfacial heat transfer coefficient in hot stamping of Al-Si coated 22MnB5 steel. Appl Therm Eng 2024;236:121604. https://doi.org/10.1016/j.applthermaleng.2023.121604.

[17] Bai Q, Lin J, Zhan L, Dean TA, Balint DS, Zhang Z. An efficient closed-form method for determining interfacial heat transfer coefficient in metal forming. Int J Mach Tool Manuf 2012;56:102–10. https://doi.org/10.1016/j.ijmachtools.2011.12.005.

[18] Xiao W, Wang B, Zheng K, Zhou J, Lin J. A study of interfacial heat transfer and its effect on quenching when hot stamping AA7075. Arch Civ Mech Eng 2018;18: 723–30. https://doi.org/10.1016/j.acme.2017.12.001.

[19] Mendiguren J, Ortubay R, De Argandona ES, Galdos L. Experimental characterization of the heat transfer coefficient under different close loop controlled pressures and die temperatures. Appl Therm Eng 2016;99:813–24. https://doi.org/10.1016/j.applthermaleng.2016.01.133.

[20] Caron EJFR, Daun KJ, Wells MA. Experimental heat transfer coefficient measurements during hot forming die quenching of boron steel at high temperatures. Int J Heat Mass Transf 2014;71:396–404. https://doi.org/10.1016/j.ijheatmasstransfer.2013.12.039.

[21] Dong S, Shan Z, Lin F, Yang H, Liang X. Determination of interfacial heat transfer coefficient at the frozen sand mold casting process of ZL101 alloy. J Mater Sci Technol 2024;194:28–42. https://doi.org/10.1016/j.jmst.2024.01.032.

[22] Wu Y, Fan R, Qin Z, Chen M. Shape controlling and property optimization of TA32 titanium alloy thin-walled part prepared by hot forming. Trans Nonferrous Met Soc China 2021;31:2336–57. https://doi.org/10.1016/S1003-6326(21)65658-3.

[23] Zhang K, Shao Z, Robson J, Huang Y, Zheng J, Jiang J. Achieving high ductility and strength in magnesium alloy through cryogenic-hot forming. J Magnes Alloy 2023; 11:3130–40. https://doi.org/10.1016/j.jma.2023.09.002.

[24] Piao YN, Jia HL, Zha M, Ma PK, Gao D, Yin CR, et al. The effect of quenching rates on microstructure and mechanical properties of an Al-Si-Cu-Mg alloy. Mater Charact 2023;196:112609. https://doi.org/10.1016/j.matchar.2022.112609.

[25] Rigas N, Lypchanskyi O, Prahl U, Merklein M. Ultrasound-assisted material characterization: an innovative method for the non-destructive in-situ detection of microstructural changes of high-strength aluminum alloys. J Mater Process Technol 2024;325:118282. https://doi.org/10.1016/j.jmatprotec.2023.118282.

[26] Xiao H, Wang Z, Geng J, Zhang C, Li Y, Yang Q, et al. Precipitation and crystallographic relationships of nanosized η/η' precipitates at S-Al interface in Al-Zn-Mg-Cu alloy. Scr Mater 2022;214:114643. https://doi.org/10.1016/j.scriptamat.2022.114643.

[27] Yang X, Liu X, Heli L, Politis DJ, Leyvraz D, Wang L. Experimental and modelling study of friction evolution and lubricant breakdown behaviour under varying contact conditions in warm aluminium forming processes. Tribol Int 2021;158: 106934. https://doi.org/10.1016/j.triboint.2021.106934.

[28] Omer K, Abolhasani A, Kim S, Nikdejad T, Butcher C, Wells M, et al. Process parameters for hot stamping of AA7075 and D-7xxx to achieve high performance aged products. J Mater Process Technol 2018;257:170–9. https://doi.org/10.1016/j.jmatprotec.2018.02.039.

[29] Zhu Q, Wu X, Cao L, Zou Y, Song H, Liu Y, et al. Precipitation evolution of Al-Zn-Mg-Cu-(Ag) alloys with a low Zn/Mg ratio. J Mater Sci Technol 2024;195:177–96. https://doi.org/10.1016/j.jmst.2023.12.071.

[30] Geng Y, Zhang D, Zhang J, Zhuang L. Early-stage clustering and precipitation behavior in the age-hardened Al–Mg–Zn(-Cu) alloys. Mater Sci Eng A 2022;856: 144015. https://doi.org/10.1016/j.msea.2022.144015.

[31] Feng Z, Liu C, Ma P, Yang J, Chen K, Li G, et al. Initial holding time dependent warm deformation and post-ageing precipitation in an AA7075-T4 aluminum alloy. J Mater Process Tech 2021;294:117111. https://doi.org/10.1016/j.jmatprotec.2021.117111.

[32] Ren Y, Wan T, Xu S, Zhang K, Zhang M, Li J. Effects of stress aging treatment on the microstructure, mechanical properties and electrochemical corrosion behavior of Al-Zn-Mg-Cu alloy. J Alloys Compd 2024;997:174686. https://doi.org/10.1016/j.jallcom.2024.174686.

[33] Lee SH, Ahn TY, Il Baik S, Seidman DN, Lee SJ, Lee YK, et al. Unravelling precipitation behavior and mechanical properties of Al–Zn–Mg–Cu alloy. J Mater Sci Technol 2025;204:177–89. https://doi.org/10.1016/j.jmst.2024.03.021.

[34] Ha S, Kayani SH, Lee K, Park S, Choi H, Seol JB, et al. Microscopic-plastic deformation behavior of grain boundary precipitates in an Al–Zn–Mg alloy. J Mater Res Technol 2024;30:3420–9. https://doi.org/10.1016/j.jmrt.2024.04.044.

[35] Liu X, Cai Z, Ming M, Hou Q, Luan X, Liu H, et al. Fast light alloy stamping technology (FAST) for manufacturing lightweight pressings from dissimilar aluminium alloy-tailor welded blanks. J Manuf Process 2024;120:1141–56. https://doi.org/10.1016/j.jmapro.2024.05.021.

[36] Lu J, Song Y, Zhou P, Xu H, Liu Y, Hua L. Effect of thermal strain on the microstructure evolution and post-aging mechanical properties of Al-Zn-Mg-Cu alloy in simulating hot stamping process. Mater Sci Eng A 2023;880:145316. https://doi.org/10.1016/j.msea.2023.145316.

[37] Li Y, Wang Y, Lu B, Yu W, Wang H, Xu G, et al. Effect of Cu content and Zn/Mg ratio on microstructure and mechanical properties of Al–Zn–Mg–Cu alloys. J Mater Res Technol 2022;19:3451–60. https://doi.org/10.1016/j.jmrt.2022.06.059.